A&A 501, 539–551 (2009)
DOI: 10.1051/0004-6361/200912108

Astronomy & Astrophysics

The RMS survey

6 cm continuum VLA observations towards candidate massive YSOs in the northern hemisphere⋆

J. S. Urquhart[1,2], M. G. Hoare[1], C. R. Purcell[3], S. L. Lumsden[1], R. D. Oudmaijer[1], T. J. T. Moore[4], A. L. Busfield[1], J. C. Mottram[1,5], and B. Davies[1]

[1] School of Physics and Astronomy, University of Leeds, Leeds, LS2 9JT, UK
e-mail: jsu@ast.leeds.ac.uk
[2] Australia Telescope National Facility, CSIRO, Sydney, NSW 2052, Australia
[3] Jodrell Bank Centre for Astrophysics, University of Manchester, Oxford Road, Manchester, M13 9PL, UK
[4] Astrophysics Research Institute, Liverpool John Moores University, Twelve Quays House, Egerton Wharf, Birkenhead, CH41 1LD, UK
[5] School of Physics, University of Exeter, Exeter, EX7 4QL, UK

Received 19 March 2009 / Accepted 17 April 2009

ABSTRACT

Context. The Red MSX Source (RMS) survey is an ongoing multi-wavelength observational programme designed to return a large, well-selected sample of massive young stellar objects (MYSOs). We have identified ∼2000 MYSO candidates located throughout the Galaxy by comparing the colours of MSX and 2MASS point sources to those of known MYSOs. The aim of these follow-up observations is to identify other objects with similar colours such as ultra compact (UC) HII regions, evolved stars and planetary nebulae (PNe) and distinguish between genuine MYSOs and nearby low-mass YSOs.
Aims. To identify the populations of UCHII regions and PNe within the sample and examine their Galactic distribution.
Methods. We have conducted high resolution radio continuum observations at 6 cm towards 659 MYSO candidates in the northern hemisphere ($10^\circ < l < 250^\circ$) using the Very Large Array (VLA). These observations have a spatial resolution of ∼1–2″ and typical image rms noise values of ∼0.22 mJy – sensitive enough to detect a HII region powered by B0.5 star at the far side of the Galaxy. In addition to these targeted observations we present archival data towards a further 315 RMS sources extracted from a previous VLA survey of the inner Galaxy.
Results. We present the results of radio continuum observations made towards 974 MYSO candidates, 272 (∼27% of the observed sample) of which are found to be associated with radio emission above a 4σ detection limit (∼1 mJy). Using results from other parts of our multi-wavelength survey we separate these RMS-radio associations into two distinct types of objects, classifying 51 as PNe and a further 208 as either compact or UC HII regions. Including all HII regions and PNe identified either from the literature or from the multi-wavelength data these numbers increase to 391 and 79, respectively. Using this well selected sample of HII regions we estimate their Galactic scale height to be 0.6°. In addition to the RMS-radio associations we are able to set upper limits on the radio emission of ≤1 mJy for the 702 non-detections, which is below the level expected if they had already begun to ionise their surroundings.
Conclusions. Using radio continuum and archival data we have identified 79 PNe and 391 HII regions within the northern RMS catalogue. We estimate the total fraction of contamination by PNe in the RMS sample is of order 10%. The sample of HII regions is probably the best representation to date of the Galactic population of HII regions as a whole.

Key words. radio continuum: ISM – stars: formation – stars: early-type – stars: pre-main sequence

1. Introduction

Massive young stellar objects (hereafter MYSOs) are one of the earliest phases in the life of OB stars when fusion has most likely started in the core, but they have not yet begun to ionise their surroundings to form an HII region. They possess strong ionised stellar winds and drive powerful bipolar molecular outflows. This brief ($\sim 10^{4-5}$ years) phase is clearly crucial to our understanding of how these massive young stars form since during this time any ongoing accretion will be disrupted and the final mass of the star may be set. In addition, the winds, outflows and eventual HII regions have an important feedback role in the fate of the rest of the molecular cloud and subsequent generations of high-mass star formation (e.g., Moore et al. 2007; Urquhart et al. 2007c; Deharveng et al. 2009).

The main difficulty in studying MYSOs is their relative rarity. The ∼30 well-known MYSOs form a heterogeneous sample (Henning et al. 1984), often discovered serendipitously, and are still largely being found this way (e.g., Shepherd et al. 1998; Cesaroni et al. 1999). Unfortunately the known sample is too small to test many aspects of massive star formation theories and may be unrepresentative of the class as a whole. The obvious solution is to carry out a systematic and statistically complete search for MYSOs.

⋆ Full Tables 3–5 and Full Figs. 2, 4, and 7 are only available in electronic form at the CDS via anonymous ftp to cdsarc.u-strasbg.fr (130.79.128.5) or via http://cdsweb.u-strasbg.fr/cgi-bin/qcat?J/A+A/501/539

MYSOs are brightest in the mid- to far-infrared where most of the bolometric luminosity emerges after reprocessing by the surrounding dust cloud. Hence, any statistically complete sample must therefore be initially selected from such data. Searches for MYSOs using mid- to far-infrared data have been made using the IRAS all-sky survey (Campbell et al. 1989; Chan et al. 1996; Molinari et al. 1996; Sridharan et al. 2002), but the concentrations of massive stars within ~±2° of the Galactic plane means there is considerable source confusion due to the large IRAS beam (~2–5′ at 100 μm). The Midcourse Space Experiment (MSX) satellite recently completed a much higher spatial resolution survey (~18″) of the Galactic plane ($|b| < 5°$) at 8, 12, 14 and 20 μm (Price et al. 2001), which completely supersedes IRAS mid-infrared data. We have developed colour-selection criteria by comparing the colours of sources from the MSX and 2MASS point source catalogues to those of known MYSOs. This has delivered a sample of approximately 2000 candidate MYSOs spread throughout the Galaxy ($|b| < 5°$, Lumsden et al. 2002).

MYSOs are very red, but unfortunately several other kinds of objects have very similar infrared colours, especially compact HII regions and some planetary nebulae (PNe), post-AGB stars, dusty red supergiants as well as nearby low- and intermediate-mass YSOs. The Red MSX Source (RMS) survey is a multi-wavelength programme of follow-up observations designed to distinguish between genuine MYSOs and these other kinds of embedded or dusty objects (Hoare et al. 2005; Mottram et al. 2006; Urquhart et al. 2008b), and to compile a database of complementary multi-wavelength data with which to study their properties[1]. These include: molecular line observations to obtain kinematic distances which are crucial for calculating luminosity, and hence distinguishing between nearby low- and intermediate-mass YSOs and genuine MYSOs (Urquhart et al. 2007b, 2008a); mid-infrared imaging to identify genuine point sources, obtain accurate astrometry, and avoid excluding MYSOs located near compact and ultra-compact (UC) HII regions (e.g., Mottram et al. 2007); and near-infrared spectroscopy (e.g., Clarke et al. 2006) to distinguish between MYSOs and evolved stars.

Another aspect of the RMS follow-up campaign is to obtain high resolution radio continuum observations to identify compact HII regions and PNe that contaminate the sample. Nearby (~1 kpc) MYSOs have an integrated radio flux from their ionised stellar winds of a few mJy at most (Hoare et al. 1994; Rodriguez et al. 1994; Hoare & Muxlow 1996; Hoare 2002), whilst most compact HII regions have much greater radio fluxes (Kurtz et al. 1994; Giveon et al. 2005). High spatial resolution is needed since very often MYSOs are located close (few arcseconds) to compact HII regions and we must be sure not to exclude these since that would bias against sites of sequential star formation. Although we want to eliminate compact HII regions as confusing sources, the RMS survey will also deliver a large and well-selected sample of these too.

In a recent paper (Urquhart et al. 2007a, hereafter Paper I) we presented the results of a set of high resolution radio observations towards 826 RMS sources located in the southern hemisphere (i.e., $230° < l < 350°$). These observations were made at 4.8 and 8.6 GHz with the Australia Telescope Compact Array (ATCA)[2] and had a 4σ sensitivity of ~1 mJy and spatial resolution of ~2″. These observations resulted in radio emission being detected towards ~200 RMS sources, a detection rate of ~25%. The majority of these, due to their morphologies and location close to the Galactic mid-plane, are thought to be compact and UCHII regions. In this paper we present a set of complementary high resolution observations made with the Very Large Array (VLA) towards a further 659 RMS sources located in the northern hemisphere ($10° < l < 250°$) for which previous high resolution radio observations were not available.

The structure of this paper is as follows: in Sect. 2 we outline our source selection, observational and data reduction procedures, and present a catalogue of the radio sources detected. In Sect. 3 we introduce additional archival data and present the criterion used for associating radio emission with RMS sources. We present the results and statistical analysis in Sect. 4. In Sect. 5 we distinguish between HII regions and PNe and discuss the Galactic distributions of these two populations. Finally in Sect. 6 we present a summary of the results and highlight our main findings.

2. 6 cm radio continuum observations

2.1. Source selection

Our colour selection criteria identified ~2000 MYSO candidates spread throughout the Galaxy in a latitude range of $|b| < 5°$ (Lumsden et al. 2002). Sources toward the Galactic centre were excluded ($|l| < 10°$) due to confusion and difficulties in calculating kinematic distances. Of these, 1101 are observable by the VLA.

In order to reduce the number of observations required, and to avoid sources that have been observed as part of other programmes, we took the following steps: 1) conducted a literature search to identify and remove well known sources whose identification was clearly established; 2) we cross-matched our source list with previous high resolution surveys (i.e., Wood & Churchwell 1989; Kurtz et al. 1994; Walsh et al. 1998; Sridharan et al. 2002) eliminating sources for which data were already available; 3) conducted a nearest-neighbour search to identify small groups of sources that were close enough to be observed in a single field.

From a literature search we eliminated 127 sources including 74 evolved stars, of which 28 are identified as PNe, 18 well known sources that have previously been studied in detail, and a further 35 YSO/HII regions that have been observed as part of the four radio surveys mentioned in the previous paragraph. In addition to these sources we also excluded 315 RMS sources that are located within the region of the inner Galaxy surveyed by Becker et al. (1994) in their 5 GHz VLA survey. We present a summary of this survey and identify the radio data associated with the RMS sources within this region in Sect. 3.2. In the rest of this section we will describe the observational set up, data reduction and source extraction procedures for these targeted VLA observations.

2.2. VLA observational set up

Radio continuum observations were made during three seasons between July 2002 and May 2005 using the Very Large Array (VLA; http://www.vla.nrao.edu/) of the National Radio Astronomy Observatory[3]. The observations were made at a frequency of ~5 GHz, corresponding to a wavelength of ~6 cm.

[1] http://www.ast.leeds.ac.uk/RMS

[2] The Australia Telescope Compact Array is funded by the Commonwealth of Australia for operation as a National Facility managed by CSIRO.

[3] The National Radio Astronomy Observatory is a facility of the National Science Foundation operated under co-operative agreement by Associated Universities, Inc.

Table 1. Summary of observation dates, array configurations and numbers of sources observed.

VLA Project Id.	Date (dd/mm/yyyy)	Array Config.	Bandwidth (MHz)	Num. Obs.
AH786	23/07/2002	B	2×25	230
	25/07/2002	B	2×25	125
AH832	22/09/2003	BnA	2×50	72
	26/11/2003	B	2×50	230
	13/12/2003	B	2×50	210
AH869	13/02/2005	BnA	2×50	65
	03/05/2005	B	2×50	122
	08/05/2005	B	2×50	51

Table 2. Summary of the observational parameters.

Parameter	
Frequency	4.86 GHz
Primary beam	4.4′
Synthesised beam[a]	∼1.5″
Largest well imaged structure[a]	∼20″
Theoretical image rms	∼0.14–0.19 mJy beam^{-1}
Typical image rms[b]	0.2 mJy beam^{-1}
Image pixel size	0.3″

[a] Declination and hour angle dependent.
[b] The stated rms values have been estimated from emission free regions close to the centre of imaged fields.

Two array configurations were used; the B array for fields north of –10° declination (the majority of the observations), and where possible, the hybrid BnA array for sources south of –10° declination as it results in a more circular beam for low elevation sources. These configurations provide a spatial resolution of ∼1–2″. To improve sensitivity and reduce bandwidth smearing two separate bandpasses were used (i.e., 2IFs) located on either side of the observing frequency. The observations made in 2002 used 2×25 MHz bandwidth with all subsequent observations using a 2×50 MHz bandwidth. In Table 1 we present a summary of the observation dates, VLA project codes, array configurations and numbers of sources observed.

Sources were grouped by position into small blocks of between 8–10 sources, with each source being observed for approximately 2–3 min within the block. To correct for fluctuations in the phase and amplitude of these data, caused by atmospheric and instrumental effects, each block was sandwiched between two short observations of a nearby phase calibrator (typically 2–3 min depending on the flux density of the calibrator). The primary flux calibrator 1331+305 was observed once during each set of observations to allow the absolute calibration of the flux density. The observational parameters are summarised in Table 2.

In total 1105 observations were made towards 1068 fields, with a couple of additional observations being made towards a small number of the more complicated emission regions to improve *uv* coverage and reduce confusion. The field names and positions are presented in Table 3.

2.3. Data reduction

The calibration and reduction of these data were performed using a combination of tasks from the AIPS and Obit software packages. Raw data were first inspected by eye and obvious phase and amplitude excursions were flagged as bad. Data from each observing session was calibrated using the standard AIPS tasks[4] and a second round of automated flagging was performed using the AUTOFLAG and MEDNFLAG tasks from Obit. AUTOFLAG clips visibilities with excessive stokes I and V amplitudes, the latter of which is especially useful as most terrestrial interference is highly polarised. MEDNFLAG operates on a source-by-source basis, flagging data whose amplitude is more discrepant than a given number of sigma times the median amplitude of the data calculated in a sliding chronological window.

Calibrated data were imaged and cleaned using the Obit IMAGER task, which has several advantages over the standard AIPS IMAGR. It implements an algorithm to detect emission and automatically defines clean windows, leading to a significant reduction in the clean bias[5]. In addition, the task regrids and re-images portions of the image containing bright compact emission. By centering unresolved sources on a pixel IMAGER can accurately represent the emission by a single delta function whilst CLEANing, allowing the creation of images with high dynamic range[6]. A region equal to the size of the primary beam (i.e., 4.4′) was imaged using a pixel size of 0.3″, which was chosen to provide ∼3 pixels across the synthesised beam and resulting in image sizes of 1760×1760 pixels.

These maps were then deconvolved using a robust weighting of 0 and up to a couple of thousand cleaning components – images were CLEANed down to approximately 3σ. Finally the processed images were corrected for the attenuation of the primary beam. Due to the nature of interferometric observations the largest well-imaged structure possible at 6 cm, given the limited *uv* coverage and integration time, is ∼20″. However, many of the maps displayed evidence of large-scale emission, which, when under-sampled, can distort the processed images by producing image artifacts. These artifacts can appear as large undulations in the image intensity which are hard to remove and make identification of weak point sources embedded within extended regions of emission difficult (see Taylor et al. 1999, p. 127). Alternatively, the large-scale emission can become over-resolved and break up into irregular, or multiple component, sources that can often be confused with real sources. In order to limit the influence of large-scale emission, these fields were re-imaged, excluding the shortest baselines, which are most sensitive to extended emission from the largest angular scales.

In Fig. 1 we present a histogram of the number of observed fields as a function of their rms noise. The noise levels have been estimated from emission free regions close to the centre of the reduced images. This figure clearly shows the effect of the different frequency bandpasses used for these observations. We have truncated the x-axis at 0.5 mJy beam^{-1}, however, less than 5% of fields have noise values higher than this. Typical noise values are ∼0.2 mJy beam^{-1}, which compares well with the theoretical values. The synthesised beam parameters of the reduced maps

[4] See Sect. 4 of the AIPS cookbook, available from http://www.nrao.edu/aips
[5] See EVLA memo 116 ftp://ftp.cv.nrao.edu/NRAO-staff/bcotton/Obit/autoWindow.pdf
[6] See EVLA memo 114 ftp://ftp.cv.nrao.edu/NRAO-staff/bcotton/Obit/autoCen.pdf

Table 3. Field positions and restoring beam parameters.

Field Name	RA (J2000)	Dec (J2000)	Field rms (mJy)	Beam size Maj × Min (PA) (″, ″, °)
G010.0026−02	01:13:01.73	−21:16:14.0	0.14	2.0 × 1.1 (−08.8)
G010.0712−00	01:12:37.93	−20:25:55.0	0.29	2.8 × 1.0 (+21.2)
G010.1434−00	01:12:38.54	−20:22:10.0	1.42	2.6 × 1.1 (−22.8)
G010.1960−00	01:12:39.02	−20:19:30.0	0.34	3.1 × 0.9 (+21.7)
G010.3844+02	01:12:01.51	−18:52:08.0	0.11	1.4 × 0.7 (−72.5)
G010.3920+00	01:12:26.28	−19:41:05.0	0.17	5.2 × 1.2 (−43.2)
G010.4984−00	01:12:46.66	−20:13:35.0	0.12	1.3 × 0.8 (−78.3)
G010.5067+02	01:12:02.30	−18:45:17.0	0.12	1.4 × 0.7 (−72.7)
G010.5888−00	01:12:42.09	−19:58:32.0	1.34	0.7 × 0.7 (−45.0)
G010.5960−00	01:12:49.00	−20:11:25.0	0.09	0.7 × 0.7 (+00.0)
G010.8407−03	01:13:35.33	−21:21:52.0	0.15	1.2 × 0.8 (+81.7)
G010.8837+01	01:12:16.16	−18:47:11.0	0.18	1.3 × 0.7 (−84.2)
G010.9257+01	01:12:14.60	−18:41:09.0	0.17	1.3 × 0.7 (−83.9)
G011.0054+00	01:12:25.68	−18:57:46.0	0.18	5.0 × 1.2 (−43.2)
G011.0421−01	01:12:57.42	−19:57:07.0	0.14	2.0 × 1.1 (−10.3)
G011.0909+00	01:12:33.90	−19:08:06.0	0.15	2.6 × 1.1 (−22.6)
G011.1827+03	01:11:54.38	−17:42:30.0	0.20	1.3 × 0.7 (−81.9)
G011.2230+00	01:12:34.82	−19:00:52.0	0.15	2.5 × 1.1 (−21.9)
G011.2689−00	01:12:54.00	−19:35:03.0	0.17	4.7 × 1.2 (−42.1)
G011.3161−01	01:13:02.28	−19:47:42.0	0.14	3.6 × 0.9 (+25.4)
G011.3252−01	01:13:08.86	−19:59:36.0	0.11	1.3 × 0.8 (−88.4)
G011.3743−00	01:12:55.00	−19:29:46.0	0.12	1.2 × 0.8 (−89.8)
G011.3757−01	01:13:07.36	−19:53:20.0	0.18	1.3 × 0.8 (−86.2)
G011.4136+00	01:12:36.31	−18:50:43.0	0.11	2.2 × 1.0 (+17.6)
G011.4201−01	01:13:07.79	−19:51:07.0	0.11	1.3 × 0.8 (−86.6)

Notes: Only a small portion of the data is provided here, the full table is available in electronic form at the CDS.

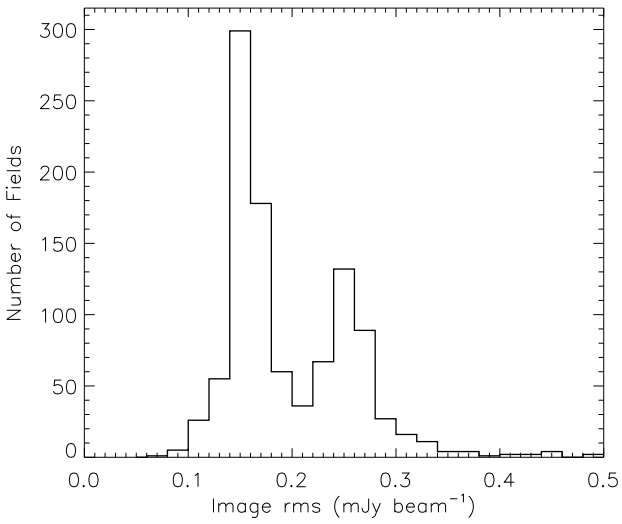

Fig. 1. Histogram of the number of fields observed as a function of map rms noise level. The double peaked distribution is a result of a smaller bandwidth used for the first season. The data has been binned using a value of 0.02 mJy beam^{-1} wide bins.

and an estimate of the maps rms noise level are presented in the last two columns of Table 3.

2.4. Source extraction and catalogue

The reduced maps were examined for compact, high surface brightness sources using a nominal 4σ detection threshold, where σ refers to the source's local rms noise level. Each source found with a peak flux above the detection threshold was visually inspected in order to distinguish between genuine sources and possible imaging artifacts, such as contamination due to bright sidelobes, which were removed from the final catalogue.

In total we have identified 669 discrete radio sources located within the 1068 fields imaged, although not all necessarily at the position of the RMS source. We name these sources using their Galactic coordinates. In Table 4[7] we present the observational parameters for each radio source, i.e., position, peak and integrated flux, and sizes of the sources' major and minor axis. In Fig. 2[7] we present continuum maps of all radio sources detected; these are presented in order of increasing Galactic longitude, are centred on the position of the radio source given in Table 4 and cover a region of 1 arcmin^2 in size. The radio source name is given above each plot and the size and shape of the restoring beam is indicated by the ellipse in the lower left corner.

Inspection of the emission maps reveal a variety of different types of morphologies. These are generally classified as: unresolved, Gaussian, spherical, core-halo, cometary, irregular and bipolar (see Churchwell 2002, for a review). Given the observed range of morphological structures a single method for extracting physical parameters is not feasible and therefore a number of methods have been employed. For sources with a fairly simple geometry (e.g., unresolved, Gaussian or spherical) we determine their positions, peak fluxes and sizes using the Miriad task *IMFIT* which fits a two component Gaussian fit to each radio source[8]. The sizes given in Table 4 are the deconvolved sizes assuming $\theta_s^2 = \theta_m^2 - \theta_b^2$ where the subscripted θ_s, θ_m and θ_b refer to

[7] Full Table 4 and Full Fig. 2 are only available in electronic form at the CDS.

[8] Miriad is a radio interferometry data reduction package. For more information see http://www.atnf.csiro.au/computing/software/miriad/.

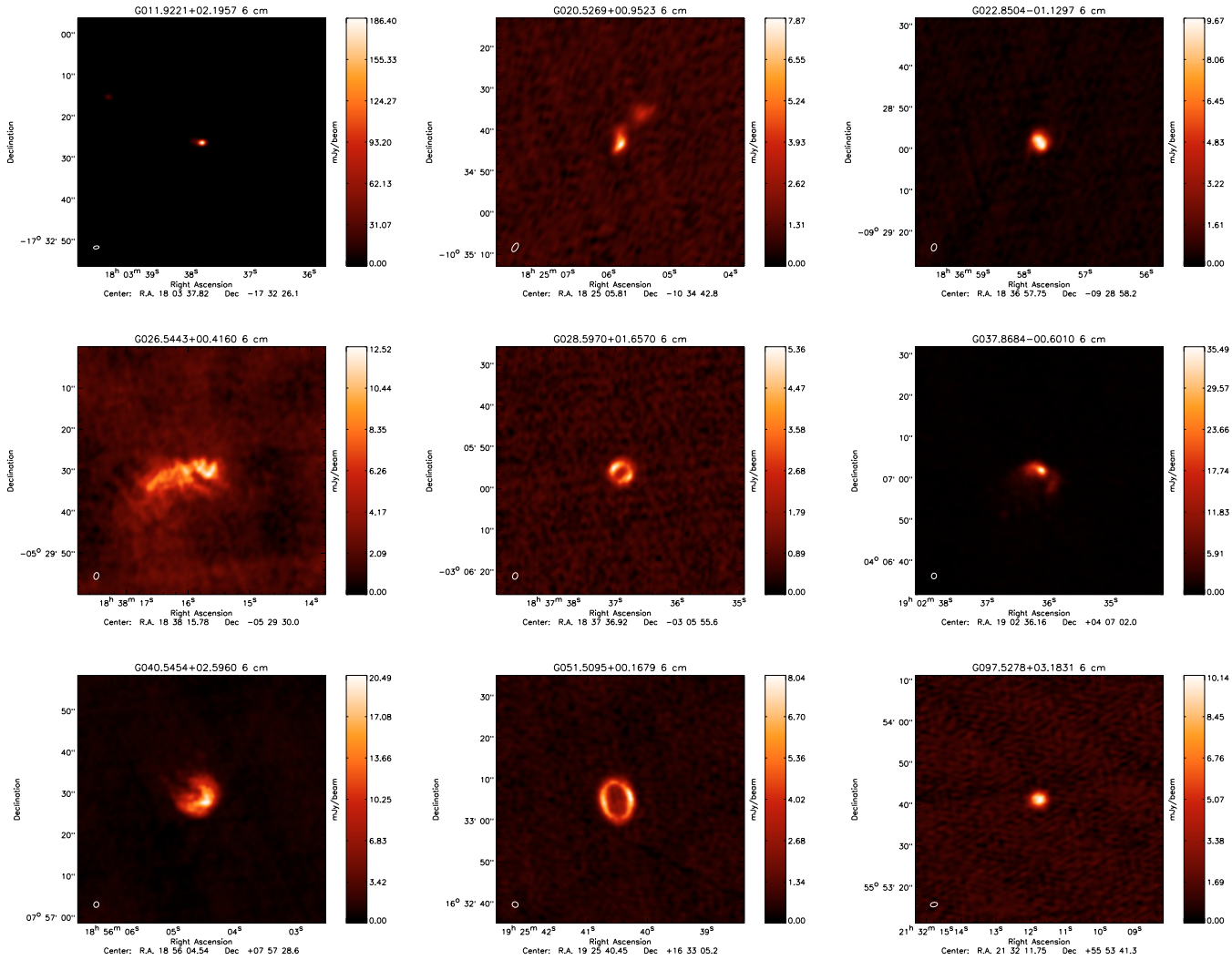

Fig. 2. Images ($1' \times 1'$) of all radio sources detected by these targeted VLA observations. The source name is printed above each image and shape and orientation of the restoring beam is shown in the lower left corner. Only a small sample of images are provided here the full version of this figure is available in electronic form at the CDS.

the deconvolved full-width at half-maximum (FWHM) size, the measured FWHM of the source, and the FWHM of the restoring beam respectively. Since the sizes of the unresolved sources (i.e., sources less than 10% larger than the beam) are very uncertain we have set an upper limit to their size which is half the FWHM of the restoring beam. Furthermore, the unresolved sources tend to be very weak and are not particularly well fit by the two component Gaussian, leading to large uncertainties in the integrated fluxes; we have therefore set the integrated fluxes to be same as the peak fluxes for the unresolved sources.

For all other morphological types the peak and integrated fluxes have been determined by summing the flux within a carefully fitted polygon around each source. For sources classified as having a shell-like morphology their position is given as the centre of the shell and the minimum and maximum correspond to the inner and outer diameters of the shell as measured at the half power points, for core-halo morphologies the major and minor axes of the core have been given. For sources with extended, irregular or cometary morphologies their sizes have been determined by eye. As all of these morphological types are extended with respect to the beam their sizes have not been deconvolved with the beam.

The radio sources detected consist of two distinct populations; thermal emission from Galactic sources such as HII regions and PNe, and an extragalactic population of non-thermal emission (e.g., active-galactic nuclei). Cross matching these radio sources with the MSX point source catalogue we find approximately a third are associated with mid-infrared emission and therefore likely to be Galactic in origin. (In the last two columns of Table 4 we present the positional offset between the radio and MSX positions and the MSX point source name.) Two-thirds of the radio sources detected have no thermal counterpart. These radio sources maybe associated with with a relatively weak thermal source not detected by MSX. Giveon et al. (2005) estimated the MSX catalogue to be ≥80% complete for thermal sources, and therefore the majority of the unassociated radio sources are like to be extragalactic in origin.

It is the radio detections associated with the RMS sources that are of most interest to us and which will be the focus for the rest of this paper. The other radio detections will not be

Table 4. VLA radio detection catalogue.

Radio Name	RA (J2000)	Dec (J2000)	Peak (mJy)	Integrated (mJy)		Source Size (″)	MSX offset (″)	MSX name
G010.0653−02.0583	18:15:36.97	−21:13:21.2	2.5	10.8		3.2 × 2.3		
G010.3924+00.5390	18:06:34.26	−19:41:05.3	0.7	2.2		4.6 × 2.1	2.3	G010.3930+00.5389
G010.5959−00.8734	18:12:14.95	−20:11:25.1	11.3	59.4		1.5 × 1.4	2.9	G010.5956−00.8740
G010.5971−00.3893	18:10:26.69	−19:57:22.4	8.2	22.5		2.3 × 1.4		
G010.6003−00.8320	18:12:06.21	−20:09:59.8	1.8	3.2		0.8 × 0.4		
G010.6161−00.3921	18:10:29.65	−19:56:27.5	32.8	99.1		2.4 × 1.5		
G010.6221−00.3788	18:10:27.42	−19:55:45.3	42.6	104.1		2.8 × 0.8		
G010.6234−00.3838	18:10:28.69	−19:55:50.1	212.2	1055.0		3.3 × 2.2	1.5	G010.6235−00.3834
G010.6240−00.3812	18:10:28.19	−19:55:43.6	33.6	86.6		1.9 × 1.6	8.3	G010.6235−00.3834
G011.1073+00.4272	18:08:27.60	−19:06:52.5	1.2	1.6		1.7 × 0.6		
G011.4201−01.6819	18:16:56.89	−19:51:08.1	0.8	3.2		1.9 × 1.5	1.1	G011.4201−01.6815
G011.6218+01.1804	18:06:44.19	−18:17:56.0	4.3	4.7		0.5 × 0.4		
G011.8724+02.2273	18:03:24.77	−17:34:06.0	3.8	4.9		0.9 × 0.3		
G011.9221+02.1957	18:03:37.82	−17:32:26.2	189.2	340.9		1.0 × 0.7		
G011.9278+02.1917	18:03:39.40	−17:32:15.1	26.7	45.2		1.0 × 0.4		
G012.1098+01.2250	18:07:34.31	−17:51:03.3	3.3	4.6		1.9 × 0.8		
G012.1175+01.1965	18:07:41.54	−17:51:28.9	32.2	63.6		1.9 × 1.5	1.2	G012.1177+01.1966
G012.4180+00.5038	18:10:51.08	−17:55:49.5	3.5	6.2		1.4 × 1.2		
G012.4317−01.1112	18:16:51.23	−18:41:28.4	8.1	105.2		3.7 × 3.1	2.2	G012.4314−01.1117
G012.8162+00.5576	18:11:27.53	−17:33:20.1	7.7	9.3		0.5 × 0.1		
G012.8616+00.8776	18:10:22.50	−17:21:41.5	1.6	1.8		0.8 × 0.2		
G012.9630+00.9441	18:10:20.15	−17:14:26.2	1.2	1.2	<	2.2 × 0.6		
G012.9712+00.9055	18:10:29.63	−17:15:07.4	1.3	1.3	<	2.2 × 0.6	10	G012.9731+00.9036
G013.1178+04.1527	17:58:58.77	−15:32:14.3	30.2	70.2		2.2 × 2.0	7.9	G013.1172+04.1507
G013.4895−00.7408	18:17:35.67	−17:35:04.0	2.9	5.1		1.9 × 0.8		

Notes: Only a small portion of the data is provided here, the full table is available in electronic form at the CDS.

discussed further, however, we present their measured parameter and emission maps in Table 4 and Fig. 2 respectively as they may prove useful to the wider community.

3. Identifying RMS-radio associations

3.1. VLA observations

Within these fields are located 1125 sources which passed our initial MSX colour selection, however, 466 were later excluded either because they were subsequently found to be associated with 2MASS sources that possess flat, or blue, near-infrared colours, or were found to be considerably extended rather than point sources in the MSX images and therefore more likely to be HII regions than MYSOs. Therefore the VLA observations presented here provide radio continuum data for the 659 RMS sources that remain from the original RMS catalogue of ∼2000 MYSO candidates. In order to identify radio sources that are associated with our RMS sources we compared the positions of the radio detections with the positions of the 659 RMS sources within the observed fields. We found a total of 167 radio sources within an initially generous 25″ search radius of 143 RMS sources.

3.2. Archival data

As previously mentioned these targeted observations were tailored to avoid a large region of the Galactic plane that had previously been surveyed by Becker et al. (1994) with the VLA. This survey covers the inner Galaxy ($350° < l < 42°$ and $|b| < 0.4°$) with a resolution of ∼6″ (9″ × 4″ restoring beam) and a median sensitivity of ∼0.18 mJy, however, similarly to the targeted observations, approximately 5% of their fields have noise levels that exceed this value by more than a factor of two. This survey was recently reprocessed using improved phase calibration and incorporating some re-observed fields (White et al. 2005). These improvements resulted in a more uniform survey and an almost three fold increase in the number of sources detected from 1272 to 3283.

We searched the White et al. (2005) catalogue for possible radio matches for the 315 RMS sources that are located within this survey region. This search identified ∼250 radio sources within a 25″ of 149 RMS sources. In order to compare the spatial distribution of the potential radio sources matched with the RMS sources we obtained images from the The Multi-Array Galactic Plane Imaging Survey (MAGPIS) project page[9].

3.3. Selection criterion

In the previous two subsections we used a rather generous search radius of 25″ to identify possible RMS-radio associations. Using this radius we identifed a total of 417 radio sources positionally coincident with 292 RMS sources. However, due to the size of the search radius there is a non-negligible possibility of chance alignments due to line of sight contamination, and therefore not all of these are likely to be genuine associations. In order to try to distinguish between real and chance associations we examined the angular correlation between the RMS and radio sources to derive an association criterion. We present a histogram plot of the angular separation between the radio sources and their nearest RMS source in Fig. 3.

The distribution of the angular separation between the radio and RMS matches illustrates the tight correlation between the two at small angular offsets. The distribution is strongly peaked at ∼1–3″ with typical separations of ∼2″, which is comparable to the positional accuracy of the MSX point source catalogue

[9] http://third.ucllnl.org/gps/

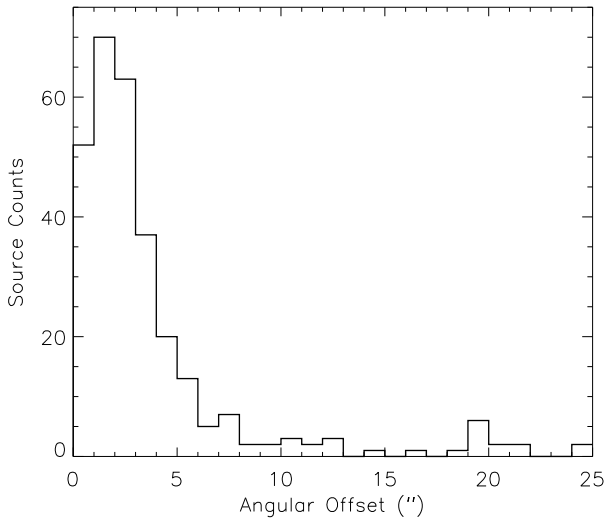

Fig. 3. Histogram of the projected angular separations between the RMS sources and their nearest radio source. The radio sources have been drawn from the targeted VLA observation and those found in the White et al. (2005) catalogue. The data have been binned using a value of 1″.

(~2″, Egan et al. 1999). After peaking sharply the distribution falls off steeply to ~6″ and then more slowly until ~13″, after which the distribution tails off completely. This distribution closely matches the distribution found towards a sample of southern RMS-radio associations observed with the ATCA (cf. Fig. 2 from Paper I).

We consider the point at which the distribution tails off to mark the transition between real associations and chance alignments. The distribution begins to flatten out between 8″ and 15″ and the selection of a cutoff point between these values is quite arbitrary. We have therefore selected a radius of 12″ for reliable associations of radio and RMS sources. We choose this value because it is the mid-point between the tail of the distribution and for consistency with the cutoff used for the ATCA observations (Paper I).

Applying this radial cutoff we find over 90% of the matched sources are located within 12″ of each other, and more than 85% of these are located within a 5″ radius. In order to check whether our cutoff radius was giving reliable associations we followed the procedures described by Giveon et al. (2005) for identifying radio-infrared matches. This analysis resulted in a reliability of 97% or better for every RMS source matched with a radio source within a 12″ radius.

4. Results and analysis

4.1. RMS-radio associations

In total 974 RMS sources are located within either the VLA fields observed as part of our programme of targeted observations or lie within the region of the plane reported by White et al. (2005, see Sect. 3.2). Searching the catalogues associated with these two programmes we find radio emission associated with 272 of the 974 RMS sources for which data is availablle. These associations amount to ~27% of the RMS sample observed (hereafter we will refer to these as RMS-radio matches). In about 20% of case we find two or more radio sources are found to be associated with a single RMS source; this brings the total number of radio source that lie within a 12″ radius (see previous section) of an RMS source to 342. In Table 5 we present the MSX names of the sources, the radio name, the angular offset, peak and integrated fluxes, angular sizes and source classifications (see Sect. 5.1 for discussion concerning source classification).

In Fig. 4 we present contour maps of the distribution of radio emission found towards all of RMS-radio matched sources. As with Paper I, the contour levels in each map have been determined using the dynamic range power-law fitting scheme described by Thompson et al. (2006). The advantage of this scheme over a linear scheme is in its ability to emphasise both emission from diffuse extended structures with low surface brightness and emission from bright compact sources. The contour levels were determined using the following relationship $D = 3 \times N^i + 4$, where D is the dynamic range of the map (defined as the peak brightness divided by the map's rms noise), N is the number of contours used (6 in this case), and i is the contour power-law index. Note this relationship has been altered slightly from the one presented by Thompson et al. (2006) so that the first contours start at 4σ rather than 3σ used by them. The lowest power-law index used was one, which resulted in linearly spaced contours starting at 4σ and increasing in steps of 3σ.

The integrated flux values range from ~1.3 mJy up to several Jy, significantly above what would be expected from an ionising stellar wind (~1 mJy at 1 kpc, Hoare 2002). These sources are therefore unlikely to be genuine MYSOs and more likely to consist of embedded compact and UCHII regions, and a small number of PNe. However, to avoid the possibility that a small number of these detections are actually due to ionised stellar winds in nearby sources we will, once the high resolution far-infrared data and reliable distances becomes available, use the ratio of the radio and infrared luminosities (i.e., Log $L_{\rm radio}/L_{\rm IR}$, see Fig. 6 of Hoare et al. 2007) and retrospectively apply the following criteria: UCHII region >8, ionised stellar wind <8. Although this works well for sources with luminosities $>10^4$ $L_\odot$, it is not so clear cut for weaker B stars where infrared spectroscopy will be needed to distinguish between stellar winds and UCHII regions.

Although this effectively eliminates a quarter of the RMS sources observed, we are still left with a large sample of MYSO candidates (702 sources or 72% or the sample), and this is after eliminating two major sources of contamination.

4.2. Detection statistics

The overall fraction of RMS sources with detected radio emission is similar to the fraction found from the ATCA observations of southern sources (~25%). However, breaking down the percentages between the two catalogues we find a significantly higher fraction of matches are found in the White et al. (2005) catalogue, i.e., the RMS-radio matches from the targeted VLA observations ~19.3% compared to 46.5% matched using White et al. (2005) catalogue.

There are two reasons for the large difference in detection rates. Firstly, the White et al. (2005) survey region covers the busiest part of the Galactic mid-plane where the majority of MYSOs and UCHII regions are expected to be found – the scale height of massive stars is ~0.5° (Reed 2000). Moving out of the mid-plane to higher latitudes the sample is likely to contain a higher proportion of evolved stars which have a much broader latitude distribution. Secondly, the targeted VLA observations, due to the array configuration and the limited uv coverage, are in theory only sensitive to angular scales of ~20″, however, the Becker et al. (1994) 6 cm survey, which mainly used the

Table 5. Parameters for radio sources found to be associated with RMS sources.

RMS Name	Radio Name[a]	Offset (″)	RA (J2000)	Dec (J2000)	Peak (mJy)	Integrated (mJy)	Source Size (″)	Classification[a]
G010.4413+00.0101	G10.440+0.011†	4.4	18:08:37.93	−19:53:58.9	7.5	32.5	13.1 × 8.1	HII region
G010.5975−00.3838	G10.598−0.384†	0.6	18:10:25.59	−19:57:11.0	66.1	136.6	7.7 × 4.7	HII region
	G10.597−0.383†	6.0	18:10:25.13	−19:57:12.2	52.0	105.6	12.6 × 2.4	HII region
	G10.601−0.384†	11.8	18:10:26.03	−19:57:01.8	32.9	78.9	12.5 × 4.0	HII region
G010.6291−00.3385	G10.629−0.338†	1.2	18:10:19.25	−19:54:12.1	18.1	25.2	4.6 × 2.9	HII region
G010.9592+00.0217	G10.959+0.022†	3.2	18:09:39.35	−19:26:26.9	178.7	195.0	2.2 × 1.0	HII region
G010.9657+00.0083	G10.967+0.009†	3.6	18:09:43.31	−19:26:25.1	16.4	68.7	12.3 × 7.9	HII region
	G10.965+0.010†	5.9	18:09:42.95	−19:26:27.8	34.2	63.8	5.9 × 4.7	HII region
	G10.965+0.006†	8.3	18:09:43.64	−19:26:36.0	19.8	74.8	13.0 × 6.6	HII region
G011.1109−00.4001	G11.111−0.400†	0.3	18:11:32.30	−19:30:40.7	18.2	50.0	9.9 × 3.4	HII region
	G11.111−0.399†	6.0	18:11:31.88	−19:30:38.5	96.7	111.9	3.7 × 1.2	HII region
G011.1723−00.0656	G11.172−0.065†	3.4	18:10:24.98	−19:17:46.1	23.5	71.0	9.8 × 6.9	HII region
G011.4201−01.6815	G011.4201−01.6819	1.1	18:16:56.89	−19:51:08.1	0.8	3.2	1.9 × 1.5	HII/YSO
G011.9454−00.0373	G11.946−0.036†	5.1	18:11:53.22	−18:36:14.6	70.2	623.4	18.3 × 14.9	HII region
	G11.944−0.037†	5.1	18:11:53.20	−18:36:21.8	271.6	453.4	4.7 × 3.9	HII region
G012.1177+01.1966	G012.1175+01.1965	1.2	18:07:41.54	−17:51:28.9	32.2	63.6	1.9 × 1.5	PN
G012.1917−00.1029	G12.192−0.103†	1.0	18:12:37.95	−18:25:15.0	21.3	119.6	18.6 × 7.2	HII region
	G12.191−0.101†	7.3	18:12:37.48	−18:25:13.3	9.5	30.1	12.4 × 5.7	HII region
G012.1993−00.0342	G12.199−0.034†	3.0	18:12:23.59	−18:22:54.4	54.3	60.1	1.8 × 1.3	HII/YSO
G012.4314−01.1117	G012.4317−01.1112	2.2	18:16:51.23	−18:41:28.4	8.1	105.2	3.7 × 3.1	HII region
G012.8062−00.1987	G12.805−0.200†	5.3	18:14:13.74	−17:55:42.1	1748.5	6290.8	12.6 × 4.6	HII region
G013.2097−00.1436	G13.210−0.144†	2.4	18:14:50.05	−17:32:44.7	317.5	1017.0	9.1 × 7.8	HII region
G014.1742+00.0226	G14.175+0.024†	3.9	18:16:08.53	−16:37:06.1	21.2	96.4	11.6 × 10.0	HII region
G014.2071−00.1105	G14.207−0.110†	3.3	18:16:41.75	−16:39:12.1	11.4	60.0	13.1 × 11.1	HII region
G014.2361+00.2138	G14.237+0.212†	7.0	18:15:34.45	−16:28:27.1	30.2	35.5	2.3 × 2.2	PN

[a] Matches identified from the White et al. (2005) catalogue are identified by a superscript † added to the end of the source's radio name.
[b] RMS sources have been give one of five difference classifications: HII region, PN, YSO, HII/YSO and Other. The first three of these are obvious, however, the last two require a little explanation. The HII/YSO classification is give to MSX sources that appear to be associated with both an HII region and a YSO. The classification "Other" is given to sources that do not fit into any of the other classification.
Notes: Only a small portion of the data is provided here, the full table is available in electronic form at the CDS.

VLA C configuration, is sensitive to scales as large as ∼150″. This point is nicely illustrated in the histogram plot of the angular sizes of sources presented in Fig. 5 and in the contoured emission maps presented in Fig. 4. Figure 5 shows the geometrical deconvolved angular diameters of RMS-radio matches found from the targeted VLA observations and those found in the White et al. (2005) catalogue.

Although in theory the targeted VLA observations should have been sensitive enough to detect a source up to 20″ in size, in practice these were only sensitive to sources roughly half this size due to the snapshot nature of the observations. There are a few points to bear in mind that arise from the limited sensitivity to angular scales larger than ∼10″. First, the targeted VLA observations have effectively filtered out emission from more extended HII regions and so the number of HII regions identified should be considered a lower limit. These more extended HII regions will be identified through our programme of mid-infrared imaging (e.g., Mottram et al. 2007). Second, care must be taken when comparing the properties of the whole sample (e.g., Galactic distribution).

4.3. Upper limits for non-detections

From the point of view of identifying a large sample of MYSOs it is the RMS radio non-detections that are more interesting since they remain MYSO candidates. It is therefore useful to determine upper limits for the radio flux towards these RMS sources. In Fig. 6 we present a histogram of the measured local noise levels at the position of the RMS sources where no radio emission is detected (the noise distributions of the targeted VLA observations and the White et al. 2005, survey are also shown). The average 1σ rms noise level is ∼0.22 mJy beam^{-1} for both data sets. We have truncated the x-axis at 1 mJy beam^{-1}, however, the noise level only exceeds this for 47 sources (∼6%) of the radio non-detections.

Using a 4σ upper limit (∼1 mJy) we find these observations are sensitive enough to detect any optically thin ionised nebula around a B0.5 or earlier type star across the Galaxy (>2 mJy at ∼20 kpc, Kurtz et al. 1994). We can therefore be reasonably confident that the HII regions identified with these data presented here is complete to all *unresolved* optically thin HII regions driven by a high mass star with a luminosity of >10^4 $L_\odot$ located on the far side of the Galaxy. However, we are less sensitive, and therefore less complete, to optically thick, compact hypercompact HII regions and more extended HII regions. However, the extended HII regions will be identified by their mid-infrared emission (e.g., Mottram et al. 2007).

5. Discussion

Kinematic distances are required before we can begin to analyses the physical properties of these RMS-radio sources. We have recently published the result of ^{13}CO observations made

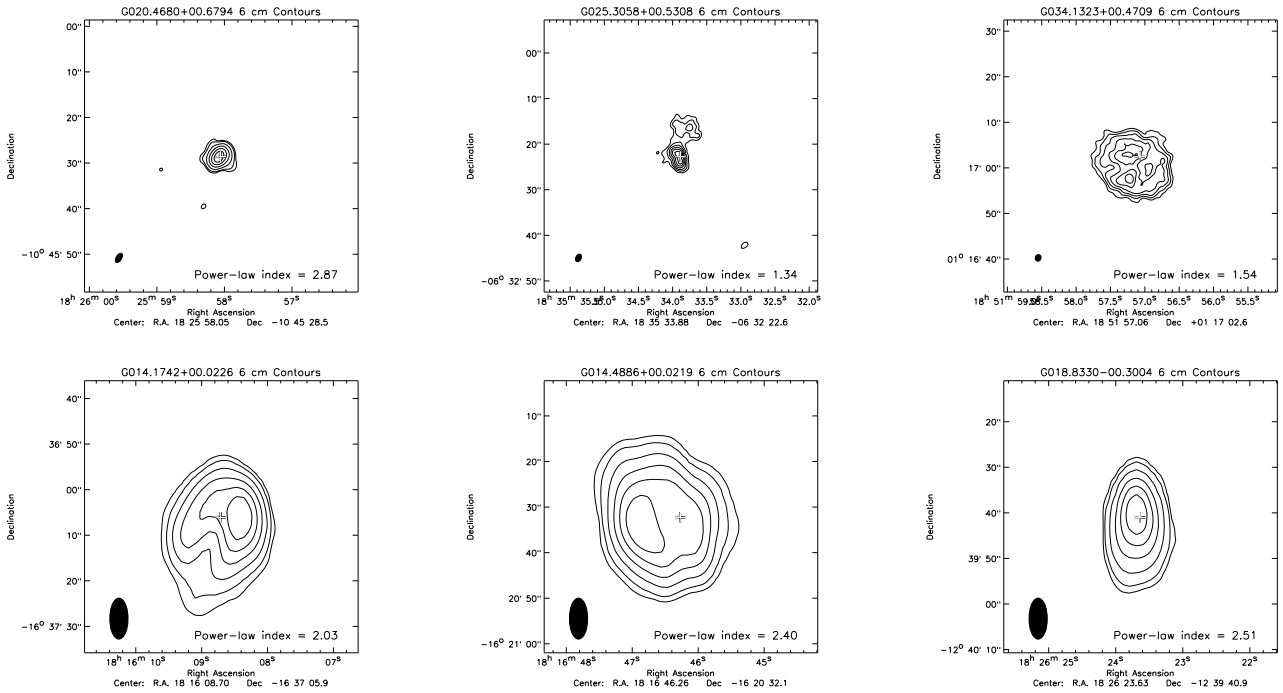

Fig. 4. Contour maps of the RMS-radio matches found from the targeted VLA observations (*upper panels*) and those found in the White et al. (2005) catalogue (*lower panels*). The first contour starts at 4σ with the intervening levels determined by a dynamic power-law which is given in the lower right corner of each plot (see text for details). The RMS name is shown above the image and the size of the synthesised beam is shown to scale in the lower left hand corner. The position of the RMS source is marked with a cross. The full version of this figure is only available in electronic form at the CDS.

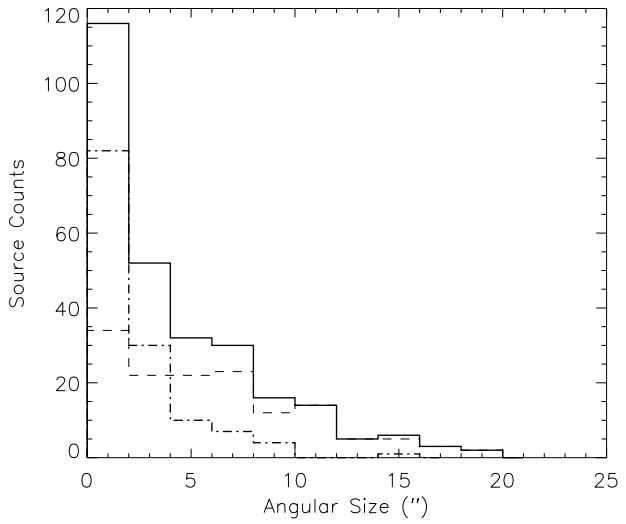

Fig. 5. Histogram plots of the deconvolved angular sizes of the radio sources associated with RMS sources. The distribution of the whole sample is indicated by the histogram outlined by a solid line. The individual angular distributions of the targeted VLA and White et al. (2005) RMS-radio matches are outlined by a dashed-dotted and dashed line respectively. These histograms have been created using a 2″ bin size.

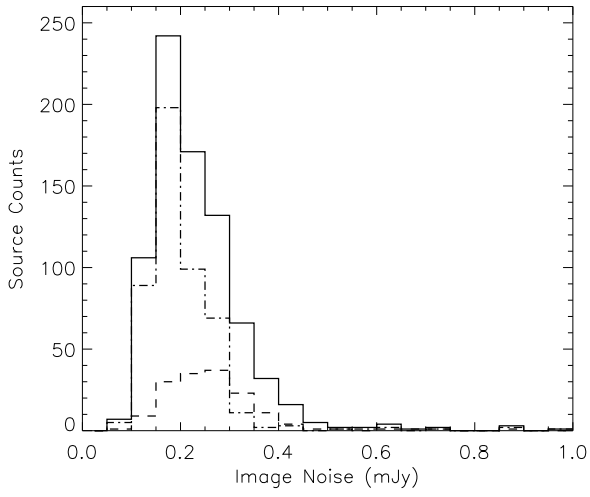

Fig. 6. Histogram plots of the noise distribution towards RMS radio non-detections. The distribution of the whole sample is outlined by a solid line while the individual noise distributions of the targeted VLA observations and the White et al. (2005) survey RMS radio non-detections matches are outlined by a dashed-dotted line and a dashed line respectively. These histograms have been created using a 0.05 mJy beam^{-1} bin size.

towards both the northern and southern hemisphere RMS sources (Urquhart et al. 2007b, 2008a), however, we were unable to unambiguously identify a velocity component to every source. Moreover, for sources located within the solar circle the Galactic rotation models give two possible distances equally spaced on either side of the tangent point; this is known as the kinematic distance ambiguity. In this paper we will therefore restrict our discussion to the investigation of the multiple radio detections, the identification of PNe and compact HII regions and their Galactic distribution.

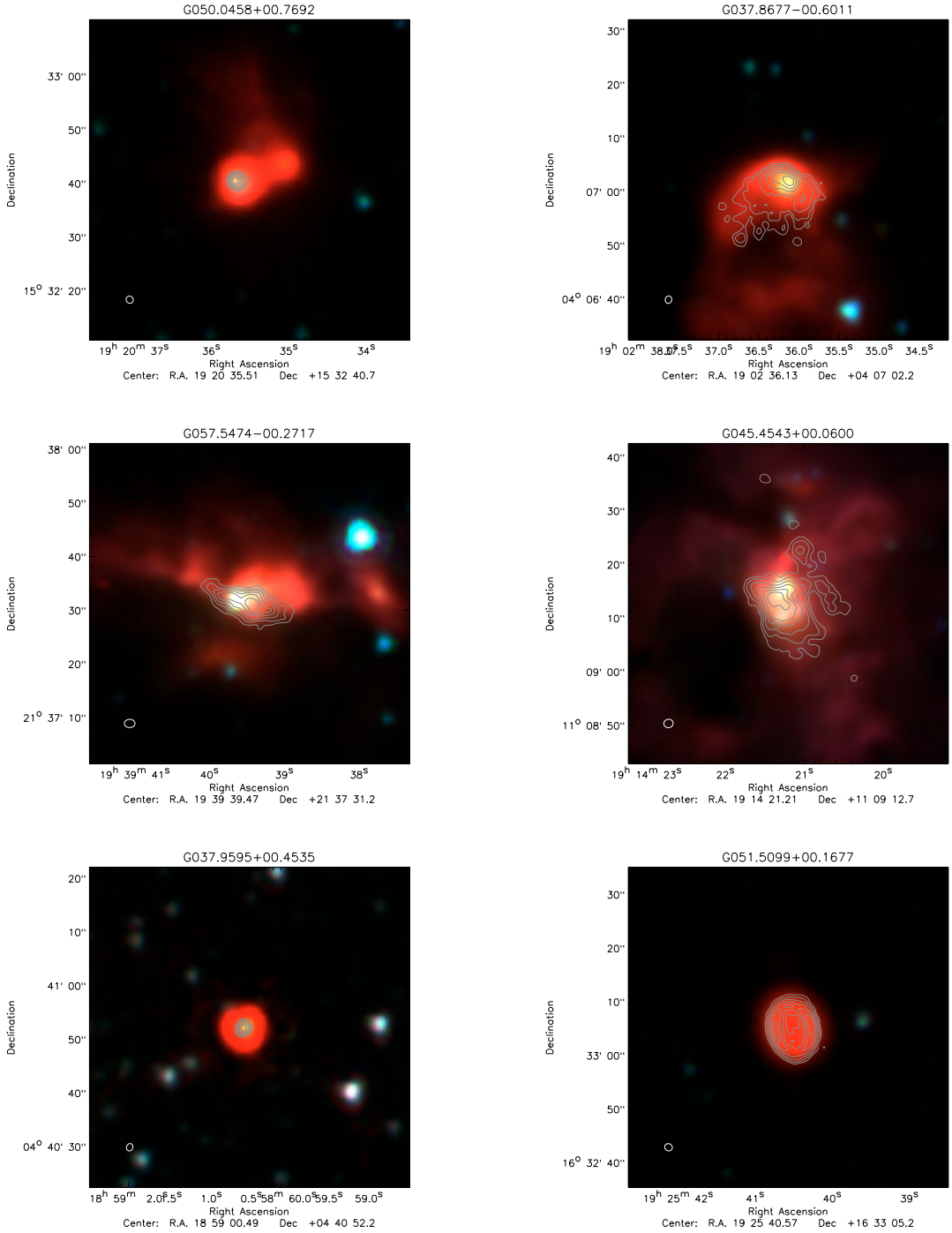

Fig. 7. Examples of the different types of radio loud RMS sources identified. In the top and centre panels we present four HII regions chosen to illustrate the difference kinds of morphologies identified and in the *bottom two panels* we present an unresolved (*left*) and resolved (*right*) PN. These images are composed of the GLIMPSE 3.6, 4.5 and 8.0 μm bands (coloured blue, green and red respectively) which are overlaid with contours of the detected radio eimission (contour levels are as for Fig. 4). The full version of this figure is only available in electronic form at the CDS.

The resolution of the MSX data is too low to effectively investigate the relationship between the mid-infrared emission from warm dust and radio emission from ionised gas. However, a large proportion of these sources are located within a region surveyed by Spitzer as part of the GLIMPSE legacy project (Benjamin et al. 2003). Therefore, for a number of these sources high resolution mid-infrared imaging data are available that allow us to study them in greater detail. We have combined the 3.6, 4.5 and 8.0 μm band images obtained with the IRAC camera (Fazio et al. 2004) to create three colour images (coloured blue, green and red respectively) for all RMS-radio matches within the region of the Northern Galactic Plane imaged by GLIMPSE ($10^\circ < l < 65^\circ$ and $|b| < 1$). We have over-plotted contours of the observed radio emission on these images in order to compare the distribution of the infrared and radio emission.

In Fig. 7 we present six examples of the two kinds of RMS-radio sources found in the sample and the different types of morphologies associated with them. We have selected these examples from the targeted VLA observations as their higher resolution is more closely matched to that of GLIMPSE data allowing the spatial features to be compared at similar resolutions. In the top and centre panels we present examples of HII regions chosen to illustrate the various types of morphologies identified (clockwise from the top left): unresolved, cometary, multipeaked and irregular. In the two bottom panels of this figure we present images of an unresolved (left) and resolved (right) PNe.

5.1. Distinguishing between HII regions and PNe

So far we have discussed RMS sources that are associated with radio emission, however, not all of these are HII regions. A small number of PNe still remain in the sample and these need to be identified and removed before we can properly investigate the distribution and statistical properties of the HII regions. The radio and MSX data alone are not sufficient to separate these two kinds of objects. However, by combining data from other parts of our multi-wavelength programme of observations it is possible to distinguish between them.

PNe have similar mid-infrared colours to UCHII regions and YSOs, and in the case of UCHII regions are both associated with radio emission. However, they, like other types of evolved stars, are not associated with large amounts of molecular gas. Hence, evolved stars and PNe are not generally associated with strong CO emission (^{12}CO $J = 1-0$ and $J = 2-1$ typically less than 1 K; Loup et al. 1993). As part of our campaign of follow-up observations we have conducted a programme of ^{13}CO observations towards all RMS sources (Urquhart et al. 2007b, 2008a). The main focus of these molecular line observations is to derive kinematic distances to the sources, which can then be used to estimate luminosities and determine galactic location. However, the non-detections also allow us to identify and eliminate a significant number of evolved stars.

Evolved stars tend to appear isolated when imaged at near and mid-infrared wavelengths and look almost identical in all wavebands (JHK and 3.6, 4.5, 5.8 and 8.0 μm), whereas YSOs and UCHIIs are often associated with nebulous emission and regions of extinction, and/or found in small clusters, which leads to observable differences in the infrared images. The final piece of information we can use to help identify evolved stars is their far-infrared spectral energy distribution (SED). Unlike the SEDs of YSOs and HII regions that both peak at approximately 100 μm, the SEDs of evolved stars tend to peak at shorter wavelengths. A number of evolved sources can therefore be identified by their IRAS fluxes, which are seen to peak at either 25 or 60 μm (Manchado et al. 1989).

Using a combination of data collected as part of the multi-wavelength programme and archival infrared images we have classified 51 of the 272 RMS-radio matches as PNe. This makes up just ~20% of the RMS-radio sample. Having removed all of the PNe we are left with a clean sample of 208 genuine compact and ultra compact HII regions. To illustrate the differences between PNe and HII regions we present examples of each in Fig. 7. These sources have been chosen as they exemplify some of the differences between the two classes of objects discuss in the previous paragraphs. The PNe are isolated and are not associated with extensive diffuse and/or irregular nebulosity, or extinction lanes, which would be expected if these were associated with molecular material. In stark contrast the HII regions are associated with large, extended regions of nebulosity, and appear to be surrounded by regions of extinction.

In the previous paragraphs we have discussed how we have distinguished between PNe and HII regions and have successfully identified 259 RMS sources as either one type or the other. However, this leaves thirteen sources so far unaccounted for. Seven of these sources have been identified as YSOs; for these sources we are currently unable to determine if the radio emission indicates the presence of a stellar wind, a radio jet or is the result of a chance alignment. Additional high resolution radio observations will be required to investigate these possibility further. The remaining six sources are an adhoc mixture of various types of radio stars and galaxies previously identified in the literature, or from inspection of the multi-wavelength data stored in the RMS database; these are classified as "Other" in Table 5[10].

5.2. Distribution of RMS-radio associations

In this subsection we examine the Galactic distributions of the PNe and HII regions. In the previous section we identified a large number of PNe and HII regions, however, to avoid any selection effects, particularly due to the filtering out of larger HII regions (see Sect. 4.2), we now include all HII regions and PNe identified either from the literature or from our multi-wavelength data. The total number of northern HII regions and PNe so far identified are 391 and 79, respectively. Our ongoing classification of sources is not yet complete as there is not yet sufficient data available to make a determination for a number of sources (~10%) and therefore these numbers may change slightly. Including the HII regions and PNe detected from the ATCA observations (Paper I) we might expect to identify ~600–800 HII regions and ~170–200 PNe in the RMS sample as a whole.

In Fig. 8 we present plots of the Galactic longitude-latitude distribution of all northern hemisphere RMS sources. In the top two panels we mark the positions of all RMS sources observed and the positions of all HII regions and PNe identified. The distribution of HII regions is strongly correlated with the Galactic mid-plane, particularly at longitudes less than 60° where all but a handful of sources can be found within 1° of the plane. This region also contains the majority of the HII regions (~70%). For longitudes larger than 50° the latitude correlation with the mid-plane becomes progressively worse and rapidly disappears. The distribution of PNe is quite different to that of the HII regions. Like the distribution of HII regions, they are also concentrated towards the inner Galaxy, however, their latitude distribution is fairly flat between $|b| < 1$ before quickly tailing off above this value.

The degree of correlation of HII regions and PNe with the Galactic mid-plane is better illustrated in Fig. 9. In this figure we present a histogram of the number of RMS sources observed as a function of Galactic latitude. In this figure we have also over-plotted the latitude distributions of the HII regions and PNe. The sample of HII regions is relatively clean of contamination, covers a broad Galactic latitude range and is more complete than previously reported samples. This sample is therefore probably the best representation to date of the Galactic population of HII regions as a whole.

Using this sample we calculate the Galactic scale height to be ~0.6°. This is in line with the values derived from the UCHII regions identified from the ATCA observations (Paper I) and by

[10] More detailed explanations concerning source classification can be found on the RMS database.

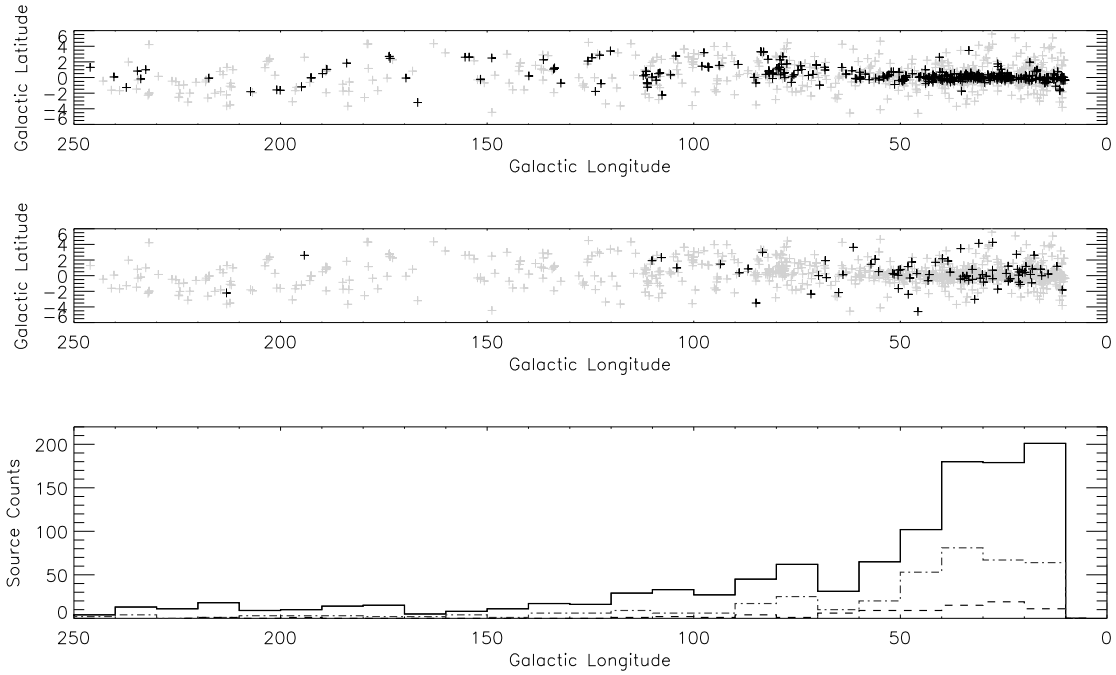

Fig. 8. Galactic distribution of all RMS sources observed as part of the targeted VLA observations or located within the region surveyed by White et al. (2005). In the *top two panels* we mark the positions of all RMS sources observed by grey crosses as a function of longitude and latitude. We indicate the positions of all HII regions and PNe by overplotting black crosses in the *top and middle panels* respectively. In the *lower panel* we present a histogram plot of the number of RMS source observed (solid line), and HII regions (dashed-dotteds line) and PNe (dashed line) detected as a function of Galactic longitude.

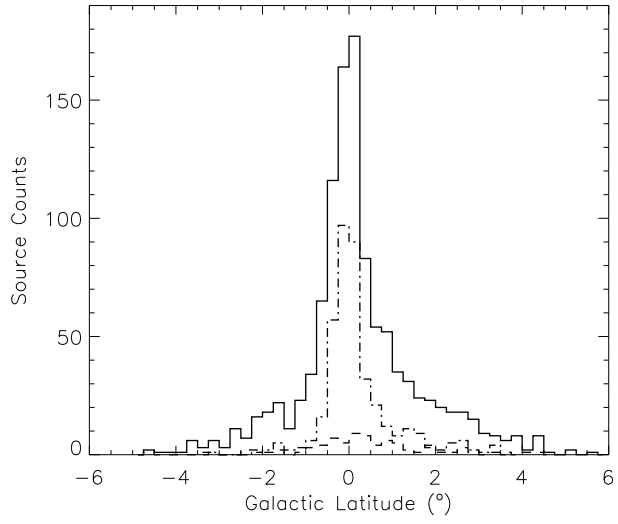

Fig. 9. Histogram plots of the latitude distributions of all northern hemisphere RMS sources, all identified HII regions and PNe are outlined by solid, dashed-dotted and dashed lines, respectively. The data has been binned in units 0.25°.

Reed (2000) from the distribution of local OB stars (~0.5°). The Gaussian FWHM of the latitude distribution is ~0.7°, which is almost three times larger than that reported by White et al. (2005) from their 6 cm survey (~0.25°), however, their survey only extended out to $|b| < 0.4°$ and so they have missed a significant number of HII regions which has led to an underestimation of the true FWHM (see also discussion by Kurtz et al. 1994).

6. Summary and conclusions

These observations form part of a multi-wavelength programme of follow-up observations of a sample of ~2000 colour selected MYSO candidates designed to distinguish between genuine MYSOs and other embedded or dusty objects. In this paper we report the results of radio continuum observations towards a sample of MYSO candidates located in the northern sky ($10° < l < 250°$). Observations were made using the VLA at a frequency of 5 GHz (~6 cm) towards 659 RMS sources. In addition to the fields observed we present archival radio data for a further 315 RMS sources obtained as part of the White et al. (2005) 6 cm survey of the inner Galactic plane.

Combining these two radio data sets provide continuum data for 974 RMS sources (~50% of the sample). These observations were aimed at identifying radio loud contaminants such as UCHII regions and PNe from the relatively radio quiet MYSOs. These observations have a typical rms noise value of ~0.2 mJy and are therefore sensitive enough to have detected an unresolved HII region powered by B0.5 or earlier type star located at the far side of the Galaxy. Our main finding are as follows:

1. The targeted VLA observations detected 669 radio sources with fluxes above a nominal 4σ cutoff (~1 mJy). Cross matching these sources with the MSX point source catalogue we find mid-infrared counterparts for approximately one third of the radio detection – these are likely to be Galactic HII regions or PNe. The remaining two-thirds of the radio detections for which no mid-infrared source could be identified are thought to consist mainly of extragalactic background objects.
2. Cross matching the VLA detections presented here, and the White et al. (2005) 6 cm catalogue, with the sample of MYSO candidates we identified 272 RMS sources that are

associated with radio emission. In total we have found that approximately ∼27% of the sample is contaminated by radio loud sources – this compares well with the results of the Australia Telescope Compact Array survey of the southern sample of MYSOs which reported a ∼25% radio association rate.

3. More interestingly from the point of view of detecting MYSOs we failed to detect any radio emission towards 702 RMS sources, and therefore after eliminating two of the main sources of contamination we are still left with a large sample of MYSO candidates. Moreover, we have measured the noise in these images and been able to place 4σ upper limits of ∼1 mJy on these non-detections.
4. Using data obtained from other parts of our multi-wavelength programme of follow-up observations and archival near-, mid- and far-infrared data we have separated the RMS-radio matches into two distinct types of objects: we have identified 208 HII regions and 51 PNe from the 272 RMS-radio matches. These numbers increase to 391 for the HII regions and 79 PNe once we include back in these types of objects previously identified in the literature which were excluded from these observations.
5. We have identified 51 PNe which is ∼20% of the radio matches, however, taking into account the PNe identified in the literature (28 PNe) and excluded from these observations we estimate the total fraction of PNe that contaminate the RMS sample is approximately 10%.
6. Using our unbiased sample of 391 compact and UCHII regions we estimate the Galactic scale height of massive stars to be 0.6°. This is in line with the values derived from the UCHII regions identified from the ATCA observations (Urquhart et al. 2007a) and by Reed (2000) from the distribution of nearby OB stars.

The radio continuum data presented here complement the observations of the southern hemisphere sample of RMS sources presented in Urquhart et al. (2007a). The full data set now includes 6 cm observations for ∼1800 MYSO candidates, and together with archival data provides radio continuum data for the entire RMS catalogue. In turn this data set forms part of a larger programme of follow-up observations of near and mid-infrared colour selected sample of MYSO candidates and are significant step in the delivery of the largest sample of MYSOs to date.

Acknowledgements. The authors would like to thank the Director and staff of the VLA for their assistance during the preparation of these observations. The authors would also like to thank the referee Michael Burton for some useful comments and suggestions. JSU is partially supported by a STFC postdoctoral grant and a CSIRO fellowship. This research would not have been possible without the SIMBAD astronomical database service operated at CDS, Strasbourg, France and the NASA Astrophysics Data System Bibliographic Services. This research makes use of data products from the MSX and 2MASS Surveys, which is are joint projects of the University of Massachusetts and the Infrared Processing and Analysis Center/California Institute of Technology, funded by the National Aeronautics and Space Administration and the National Science Foundation.

References

Becker, R. H., White, R. L., Helfand, D. J., & Zoonematkermani, S. 1994, ApJS, 91, 347
Benjamin, R. A., Churchwell, E., Babler, B. L., et al. 2003, PASP, 115, 953
Campbell, B., Persson, S. E., & Matthews, K. 1989, AJ, 98, 643
Cesaroni, R., Felli, M., & Walmsley, C. M. 1999, A&AS, 136, 333
Chan, S. J., Henning, T., & Schreyer, K. 1996, A&AS, 115, 285
Churchwell, E. 2002, ARA&A, 40, 27
Clarke, A. J., Lumsden, S. L., Oudmaijer, R. D., et al. 2006, A&A, 457, 183
Deharveng, L., Zavagno, A., Schuller, F., et al. 2009, A&A, 496, 177
Egan, M. P., Price, S. D., Moshir, M. M., Cohen, M., & Tedesco, E. 1999, NASA STI/Recon Technical Report N, 14854
Fazio, G. G., Hora, J. L., Allen, L. E., et al. 2004, ApJS, 154, 10
Giveon, U., Becker, R. H., Helfand, D. J., & White, R. L. 2005, AJ, 129, 348
Henning, T., Friedemann, C., Guertler, J., & Dorschner, J. 1984, Astron. Nachr., 305, 67
Hoare, M. G. 2002, in Hot Star Workshop III: The Earliest Phases of Massive Star Birth, ed. P. Crowther, ASP Conf. Ser., 267, 137
Hoare, M. G., & Muxlow, T. B. 1996, in Radio Emission from the Stars and the Sun, ed. A. R. Taylor, & J. M. Paredes, ASP Conf. Ser., 93, 47
Hoare, M. G., Drew, J. E., Muxlow, T. B., & Davis, R. J. 1994, ApJ, 421, L51
Hoare, M. G., Lumsden, S. L., Oudmaijer, R. D., et al. 2005, in Massive Star Birth: A Crossroads of Astrophysics, ed. R. Cesaroni, M. Felli, E. Churchwell, & M. Walmsley, IAU Symp., 227, 370
Hoare, M. G., Kurtz, S. E., Lizano, S., Keto, E., & Hofner, P. 2007, in Protostars and Planets V, ed. B. Reipurth, D. Jewitt, & K. Keil, 181
Kurtz, S., Churchwell, E., Wood, D. O. S., & Myers, P. 1994, BAAS, 26, 907
Loup, C., Forveille, T., Omont, A., & Paul, J. F. 1993, A&AS, 99, 291
Lumsden, S. L., Hoare, M. G., Oudmaijer, R. D., & Richards, D. 2002, MNRAS, 336, 621
Manchado, A., Garcia-Lario, P., Esteban, C., Mampaso, A., & Pottasch, S. R. 1989, A&A, 214, 139
Molinari, S., Brand, J., Cesaroni, R., & Palla, F. 1996, A&A, 308, 573
Moore, T. J. T., Bretherton, D. E., Fujiyoshi, T., et al. 2007, MNRAS, 379, 663
Mottram, J. C., Urquhart, J. S., Hoare, M. G., Lumsden, S. L., & Oudmaijer, R. D. 2006, ArXiv Astrophysics e-prints
Mottram, J. C., Hoare, M. G., Lumsden, S. L., et al. 2007, A&A, 476, 1019
Price, S. D., Egan, M. P., Carey, S. J., Mizuno, D. R., & Kuchar, T. A. 2001, AJ, 121, 2819
Reed, B. C. 2000, AJ, 120, 314
Rodriguez, L. F., Garay, G., Curiel, S., et al. 1994, ApJ, 430, L65
Shepherd, D. S., Watson, A. M., Sargent, A. I., & Churchwell, E. 1998, ApJ, 507, 861
Sridharan, T. K., Beuther, H., Schilke, P., Menten, K. M., & Wyrowski, F. 2002, ApJ, 566, 931
Taylor, G. B., Carilli, C. L., & Perley, R. A., 1999, Synthesis Imaging in Radio Astronomy II
Thompson, M. A., Hatchell, J., Walsh, A. J., MacDonald, G. H., & Millar, T. J. 2006, A&A, 453, 1003
Urquhart, J. S., Busfield, A. L., Hoare, M. G., et al. 2007a, A&A, 461, 11
Urquhart, J. S., Busfield, A. L., Hoare, M. G., et al. 2007b, A&A, 474, 891
Urquhart, J. S., Busfield, A. L., Hoare, M. G., et al. 2008a, A&A, 487, 253
Urquhart, J. S., Hoare, M. G., Lumsden, S. L., Oudmaijer, R. D., & Moore, T. J. T. 2008b, in Massive Star Formation: Observations Confront Theory, ed. H. Beuther, H. Linz, & T. Henning, ASP Conf. Ser., 387, 381
Urquhart, J. S., Thompson, M. A., Morgan, L. K., et al. 2007c, A&A, 467, 1125
Walsh, A. J., Burton, M. G., Hyland, A. R., & Robinson, G. 1998, MNRAS, 301, 640
White, R. L., Becker, R. H., & Helfand, D. J. 2005, AJ, 130, 586
Wood, D. O. S., & Churchwell, E. 1989, ApJS, 69, 831